Observations of gravity waves in the OH airglow layer above Rothera (68°S, 68°W) using a three-dimensional S-Transform analysis

Shaun M. Dempsey[1,2], Corwin J. Wright[1], Neil P. Hindley[1], Nicholas J. Mitchell[1,2], Tracy Moffat-Griffin[2], Pierre-Dominique Pautet[3]and Michael J. Taylor [3]

[1]Centre for Atmospheric and Oceanic Sciences, Department of Electronic and Electrical Engineering, University of Bath, Bath, UK
[2]British Antarctic Survey, Cambridge, UK
[3]Physics Department, Utah State University, Logan, Utah, USA

Key Points:

- We apply the 3D Stockwell Transform to two-dimensional time-varying airglow imagery
- The majority of waves observed are short wavelength, fast waves with short periods.
- We can determine accurate spatiotemporal locations of the waves, periods and wavelengths measured.

Corresponding author: Corwin J. Wright, `c.wright@bath.ac.uk`

Abstract

In this study, we apply the three-dimensional Stockwell Transform (3DST) to a novel dataset, namely airglow imager data from Rothera (68°S, 68°W). We use this approach to investigate small-scale high-frequency gravity waves (GWs) in the hydroxyl (OH) airglow layer, at a height ∼87 km in the mesosphere and lower thermosphere (MLT). MLT GWs are often underrepresented in models, being parameterised due to their small scale size and as such, the significant quantities of momentum and energy transferred by these small waves are missed. Better quantification of these waves is thus requried to support future model developement. We find that the 3DST can identify waves and extract wave properties and their locations. Horizontal wavelengths are observed ranging from 10 to 40 km and vertical wavelengths of 15 to 40 km, with wave periods of 5 to 9 minutes, peaking at 7.5 minutes. These values are consistent with previous studies. Group speeds are found to be non-zero and large, implying that these GWs travel horizontally and fast. This case study demonstrates that the 3DST can be applied to airglow imager data and can successfully extract GW parameters. This is an important step in automating GW analysis in airglow.

1 Introduction

Atmospheric gravity waves (GWs) are fluid-dynamical waves which propagate through the atmosphere and are critical to the dynamics, transport and circulation of the stratosphere, mesosphere and thermosphere (Fritts & Alexander, 2003; Fritts et al., 2006). They are mainly generated in the lower atmosphere by sources including mountains, convective storms, and dynamical systems such as jets, and have spatial scales of ten to hundreds of kilometres and temporal scales from five minutes to several hours.

Due to the decrease of density with height, GWs grow in amplitude as they ascend into the mesosphere and lower thermosphere, eventually overturning, breaking and depositing the energy and momentum they transport from their source into the mean flow. This deposition is sufficiently large to force a meridional flow through zonal drag, driving the mesopause temperature up to 100 K from radiative equilibrium ((Lindzen, 1981; Becker, 2012), and initiating a residual circulation from the cold summer to the warm winter pole. As global circulation models extend upwards into the mesosphere/lower thermosphere (MLT) system and beyond, they must hence be able to reproduce either GWs and/or the energy and momentum they transport accurately. Current models fail to recreate much of the GW activity responsible for controlling and determining the global circulation, as the waves exist at spatial and temporal scales which are not resolved by models of this type. To compensate for this missing effect, the waves are instead parameterised in such models. To do so effectively, the GW parametrisations must be tuned to represent the real atmosphere, accurately depicting the waves' impact on the atmosphere.

Previous observational and modelling studies have found that GW activity is particularly intense in the wintertime over the Southern Andes and the Antarctic Peninsula (Kogure et al., 2021; Hindley et al., 2015; Baumgaertner & McDonald, 2007; Alexander & Teitelbaum, 2007). This region is distinguished by steep topography, high winds over the Southern Ocean, and ferocious frontal activity, which together lead to the generation of strong orographic, convective, and jet-front GWs. As such, knowledge of the behaviour of the waves in the MLT above this region is especially important to guide future model development. This strong GW activity is well-known, and as such a wide range of wave-resolving instruments have been deployed to this region over the past few decades. Consequently, we are now able to investigate these GWs in many ways, such as satellites, rockets, balloons and ground-based techniques (Hindley et al., 2022; Perrett et al., 2021; Hindley et al., 2019; Moffat-Griffin & Colwell, 2017; Wright et al., 2017; Wüst & Bittner, 2008; Goldberg, 2004; Yoshimura et al., 2003).

One commonly-used technique for both satellite and ground-based GWs observations is to exploit atmospheric airglow. Physically, this airglow is caused by photon emissions from chemiluminescent processes which involve species such as atomic oxygen, atomic nitrogen, and hydroxyl radicals (Khomich et al., 2008). This phenomenon, also known as nightglow, acts as a passive tracer for atmospheric dynamics in the MLT, facilitating the study of GWs via imagers, rockets act satellites (e.g. Ganaie et al. (2022); Kogure et al. (2020); Hu, Ma, Yan, Hindley, Xu, and Jiang (2019a); Miller et al. (2015); Gardner and Taylor (1998); Takahashi et al. (1996); Taylor et al. (1993); Peterson (1979)).

Several energy bands contribute to the total visible and short-wave infrared airglow intensity observed at ground level, but the intensity in the short-wave infrared region is substantially higher in hydroxyl (OH) than at other infrared wavelengths. Specifically, in the short-wave infrared regime lie the Meinel bands, initially studied by Meinel (1950), which arise from rotational and vibrational atomic transitions (von Savigny, 2015). OH is the primary radiation source of the near-infrared (NIR) airglow layer, which is centred at 87 km in height and has a full-width-half-maximum of around 8 km (Baker & Stair, 1988), varying in altitude by typically a few kiolmetres (von Savigny, 2015; Wüst et al., 2016, 2022).

GWs appear in airglow layers as a result of changes in pressure and temperature caused by the waves passing through the medium, which lead to intensity fluctuations in the observed emitted radiation. Many previous studies have shown that OH airglow emissions are excellent tracers for observing atmospheric properties and studying dynamical processes such as instabilities, ripples, small-scale GWs, and larger-scale atmospheric waves such as tides and planetary waves (Sedlak et al., 2020; J. Li et al., 2017; Cao & Liu, 2016). The spectral properties of small-scale GWs in the MLT, such as wavelengths, phase speeds, and propagation directions, can hence be directly observed in the airglow layers by using optical imagers. Previous studies have observed GWs with typical horizontal wavelengths of 20-100 km, intrinsic wave periods of 5 – 10 minutes, and horizontal phase speeds ranging from 30 to 100 ms^{-1} (Ejiri et al., 2003; Taylor et al., 1997; Z. Li et al., 2011). These limits are imposed by the spatial extent airglow imagers can observe and the cadence of images taken.

In this study, we present a novel application of the three-dimensional Stockwell Transform (S-Transform) to OH airglow imager data from the British Antarctic Survey base at Rothera (68°S, 68°W), using data from the night of the 26th – 27th April 2012 as both as a case study and a demonstration of the technique. We use the S-Transform to observe wave parameters (i.e. wavelengths and periods) and then calculate meteor radar winds from the same location to compensate for the Doppler-shifting effects of the wind and establish 'intrinsic' wave parameters, i.e. in the frame of reference of the wave.

In Section 2 we describe the data sources, firstly from the airglow imager and secondly from the meteor radar. Section 3 deals, firstly, with the airglow image processing, secondly with the S-Transform analysis, thirdly with the meteor radar winds and finally with the calculation of wave parameters. Section 5 discusses our method and results in the context of previous studies. Finally, in Section 6 we provide our conclusions and a future outlook on how this semi-automated method could be applied more broadly.

2 Data

2.1 Airglow Imager

Airglow imagers have an extensive track record as a tool for detecting and characterising GWs in atmospheric airglow layers (e.g. Nielsen et al. (2009); Matsuda et al. (2014); Rourke et al. (2017)). Here, we use an all-sky (180°) monochromatic filter imaging system to observe GWs in the ∼87 km OH airglow layer. The specific instrument used measures these OH signals with a 15-second exposure period, and also measures weaker

O_2 and Na signals at 90-second and 120-second exposure periods respectively. Combined, this gives an overall measurement cadence of ~ 6 min with an embedded 2-minute OH cadence. Figure 1 illustrates the approximate emission distribution of these layers as a function of height; we use only the OH data here as proof-of-concept, but future studies could exploit these additional layers to provide 4D (i.e. distance/height/time) GW information from the same site. Similar systems have been used in past studies to analyse short-period GWs (e.g. Taylor et al. (1997); Pautet (2005); Nielsen et al. (2006))

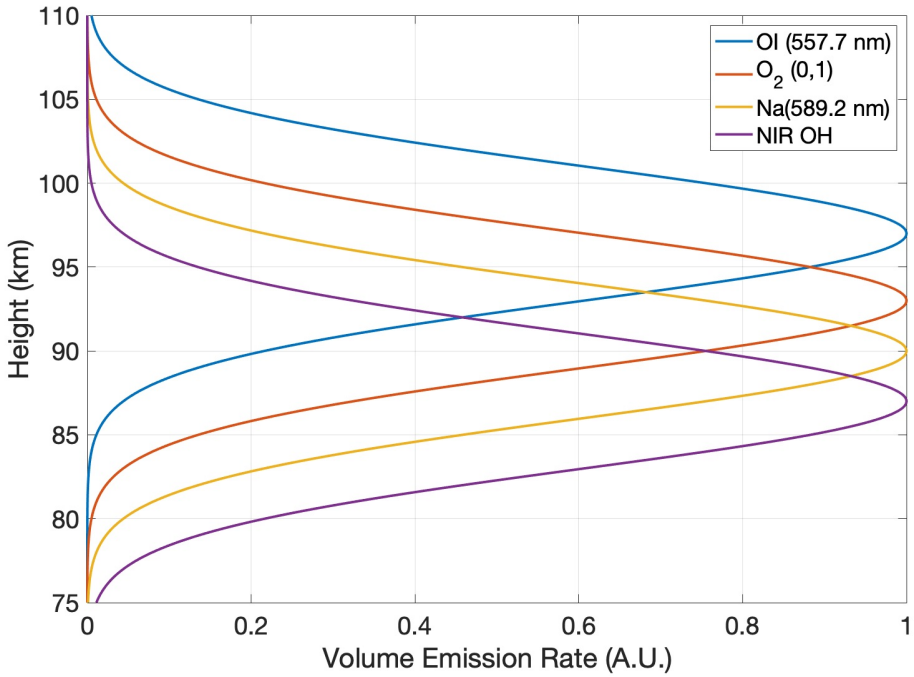

Figure 1. Diagrammatic representation of the heights and volume emission rate of four MLT airglow species. Adapted from Nielsen (2007).

2.2 Meteor Radar

Meteor radars are a well-established means of monitoring MLT winds at heights from 75 to 105 km. As such, they have been widely used for ground-based tidal and GW studies (e.g. Hindley et al. (2022); Stober et al. (2021); Dempsey et al. (2021); Davis et al. (2013); Beldon et al. (2006); Mitchell (2002)).

Here, we use a SKYiMET meteor radar located at the British Antarctic Survey base at Rothera (68°S, 68°W).

This instrument was deployed in 2005 and has been operating almost continuously from 2005 up to the present. Hocking et al. (2001) provide a full explanation of the SKiYMET radar operation.

We calculate horizontal winds from raw meteor measurements according to the method outlined by Hindley et al. (2022), combining the inferred individual horizontal velocities for each meteor using a Gaussian weighting in height and time around a specified height and time. These Gaussian weightings have full-width-half-maxima of 2 hours in time and 3 km in height. We move the centre of each Gaussian over the data in 1 hour

time and 1 km height steps, yielding winds at an hourly resolution across the height range from 75 to 105 km. This approach has previously been applied by both Dempsey et al. (2021) and Hindley et al. (2022). We use these inferred winds to convert our GW measurements from the ground-based to the intrinsic frame of reference, linearly interpolating the winds to the time of each airglow image to provide local zonal and meridional wind estimates.

3 Method

Our S-Transform GW analysis, described below, is based on a Fourier Transform algorithm and thus requires the input data to be regularly-gridded in both space and time. We also need to remove fast- and slowly-varying background features. Accordingly, the data require some preprocessing before they can be analysed. Figure 2 presents the steps in our airglow image preprocessing and processing chain. The units of the data are arbitrary brightness units recorded by the imager, but are consistent between panels.

Figure 2a shows an example raw image obtained from the instrument. GWs are visually apparent in the frame as curved striped features, but are overlaid by considerable noise from stars and from the Milky Way Galaxy, which in this frame runs through the middle of the image. In addition, as there is no geographic metadata stored by the imager other than the time of each frame, we need to produce this geographic information.

Therefore, we must first convert the observed pixel positions to a spatial location (i.e. latitude and longitude) and also remove the stars and the galaxy. The galaxy removal step is particularly important in this regard: as it is a bright rotating near-linear object, application of spectral analysis techniques are likely to identify its rotation as the wave to be studied, rather than the overlying small amplitude ripples and bands which are the our target.

3.1 Airglow Imager Geometry

We first convert coordinate frames, with the aim of geolocation each pixel in the raw data to a specific spatial distance and direction from the centre of rotation of the image, i.e. the vertical axis above the imager. For this purpose, we assume (i) that the airglow layer we are observing is at 87 km,(ii) that the zenith, i.e. directly above the Rothera airglow imager, is in the middle of the frame and (iii) that the edge of the frame represents the horizontal plane of the ground. Using the angle subtended by each pixel from the centre pixel, we can then geometrically calculate the latitude and longitude, or radius and direction, of each point in the frame.

Figure 3 presents the geometry of the airglow layer used to compute this conversion. To do this, we calculate the arc length, a, from the zenith position. Under the assumption that the airglow layer is at a height h of 87 km above the observer at P, each pixel location Q makes a right-angled triangle with angle θ subtended. This angle allows us to calculate the arc length, a, of the point Q. R_E is the radius of the Earth and $r = R_E + h$.

The first step is to calculate the location of P in the PQ plane, P^+. This is given by:

$$P^+ = (P_x^+, P_y^+) = (R_E cos\theta, R_E sin\theta) \tag{1}$$

We may use this to calculate the angle β as:

$$\beta = \phi - \alpha \tag{2}$$

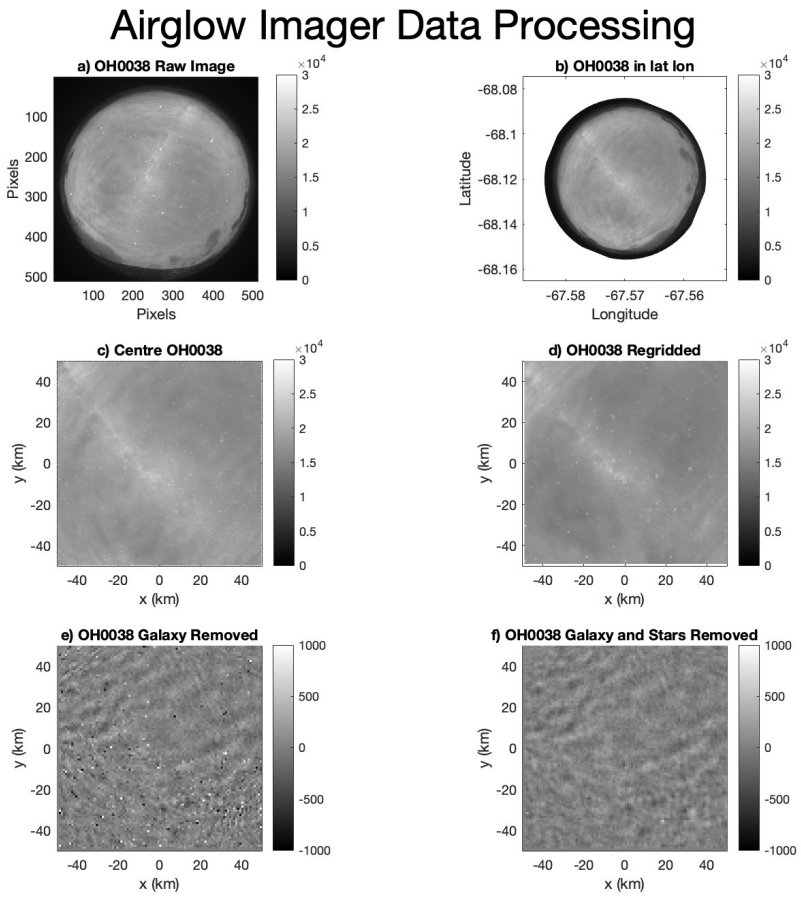

Figure 2. Processing steps of the airglow images explained for one image. Panel a) presents the raw image as given in the tif file, b) presents the image projected on a latitude/longitude grid, c) is the centre 100 km square around the zenith, d) is the centre 100 km around the zenith interpolated onto a regularly spaced grid, e) is the centre grid following the FFT galaxy removal and finally f) presents the field of view with a final step of star removal performed.

$$tan\alpha = \frac{P_x^+}{P_y^+} \tag{3}$$

$$cos\phi = \frac{P_y^+}{r} \tag{4}$$

This means that:

$$\beta = cos^{-1}\left(\frac{P_y^+}{r}\right) - tan^{-1}\left(\frac{P_x^+}{P_y^+}\right) \tag{5}$$

$$\beta = cos^{-1}\left(\frac{R_E sin\theta}{r}\right) - tan^{-1}\left(\frac{R_E cos\theta}{R_E sin\theta}\right) \tag{6}$$

The arc length is therefore given by:

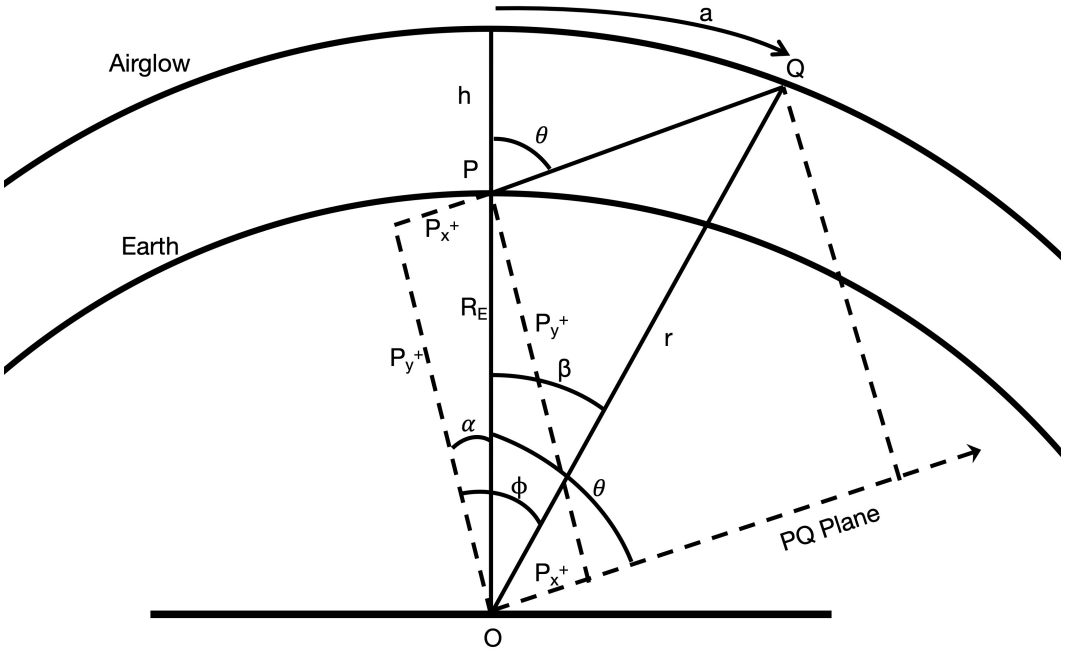

Figure 3. Geometry of airglow layer at height h above the observer at P at a given point, Q. This figure allows us to extract the arc length of a point in of the airglow given an angle subtended by a pixel from the centre of the frame.

$$a = r\beta = r\left(cos^{-1}\left(\frac{R_E sin\theta}{r}\right) + \theta - \frac{\pi}{2}\right) \tag{7}$$

Therefore the arc length can be described by:

$$a = r\beta = rcos^{-1}\left(\frac{R_E sin\theta}{R_E + h}\right) + r\left(\theta - \frac{\pi}{2}\right) \tag{8}$$

Calculating this arc length for each point allows us to calculate a distance and direction from the zenith, which in turn allows us to find the latitude and longitude of each pixel location, as shown in Figure 2b. We have removed any pixel information below the horizon in this figure, but the image still exhibits many undesirable features. For example, at the edges of the image, the features are warped due to the fisheye lens used to record these all-sky data. This data hence cannot be reliably used to measure GW properties without significant further preprocessing. To avoid this need in our proof-of-concept study, we avoid this issue by considering only a central locally-flat box.

We define this box as a square region centred at image-centre and including all areas within 100km in both the x and y directions of the image, i.e. eastwards and northwards. This centre square is shown in Figure 2c. In this image, the stars and galaxy are still visually prominent, which will significantly impact our later spectral analysis. Furthermore, our data at this stage, while on a spatial grid, are not regularly-spaced, as required for the S-Transform (or any Fourier-based) analysis. To address this, we linearly interpolate the data onto a 1 km grid in x and y. This re-gridded data is shown in Figure 2d. During this step, we also ameliorate the strong signals due to stars by identifying bright points on the image and setting the values to the average of the surrounding

pixels. Only pixels exceeding a cutoff of the 98th percentile are dealt with this way, and this does leave some stellar signatures which we address below. We can see that we have not lost any geophysical information concerning the airglow layer in this step, and the waves present in the original image can still be seen.

We now move onto the dominant background feature of the Milky Way galaxy. This is one of the most visually noticeable features of the sky, especially in dark locations such as Rothera. To remove this signal do this, we perform a three-dimensional FFT on the image and then remove low temporal frequencies, i.e. signals with long and regular temporal periods. This is done using a 3D Fast Fourier Transform, the inverse FFT returns Figure 2e, in which the signature of the galaxy has been very significantly ameliorated. The stars, however, are still present in the frame and could be identified by the S-Transform as strong waves with very short periods and wavelengths. The final step, therefore, is to more strongly remove the stars. We do this using a difference filter, where we compute the difference between adjacent pixels time, i.e. between frames. Specifically, we identify those pixels which show a difference of over 300 (in arbitrary units) between frames and remove the value, replacing it with the mean of the surrounding values. This returns Figure 2f where the processed data appears with no strong signatures of either stars or the galaxy and with the target waves now very visually prominent.

3.2 S-transform Wave Analysis

When extracting wave properties from airglow data, a conventional Fourier transform analysis can identify the frequencies present in the data; however, it cannot identify where and when these frequencies occur in geospatial coordinates. For this, another method is required. Accordingly, in this study we apply the 3-D Stockwell transform (3DST) technique described by Wright et al. (2017) and Hindley et al. (2019) to measure the spectral properties of GWs, using two dimensions of space (northwards and eastwards) and one of time. Based upon the work of R. Stockwell et al. (1996) and Hindley et al. (2016), this method provides a voxel-by-voxel estimate of the amplitude, spatial and temporal frequency and direction of propagation of the strongest wavelike signal at every location in the 3-D (i.e. x, y, t) data volume. From these estimated properties, we are further able to infer properties such as phase speed and vertical wavelength, as described below.

The S-transform has been extensively used in previous GW studies (R. G. Stockwell & Lowe, 2001; McDonald, 2012; Wright & Gille, 2013; Hindley et al., 2016; Hu, Ma, Yan, Hindley, Xu, & Jiang, 2019b; Hu, Ma, Yan, Hindley, & Zhao, 2019; Hindley et al., 2019), and demonstrated to be a highly capable technique for measuring and localising frequencies (or wavenumbers) and their associated amplitudes. However, these previous gravity wave studies have used it in spatial dimensions only, and applying it to mixed space/time data as we do here is a novel approach. By limiting the range of permitted frequencies over which the spectral windows are applied, we are also in principle able to select for different periods and wavelengths to allow the investigation of ripples and bands; however, as this study is a demonstration of the method, we have not, in this case, restricted the frequencies detected in this way.

3.3 Calculating Wave Properties

With the measured parameters from the S-Transform, supported by wind data from the meteor radar, we can calculate both observed and intrinsic wave parameters, i.e. the wave parameters in both ground-based Eulerian and wind-following Lagrangian frames of reference.

To do this, we first use the 3DST to measure the horizontal wavenumbers (k and l in the zonal and meridional directions, respectively), period, frequencies, wavelengths and amplitudes of the observed waves. From these, we can directly compute the hori-

zontal wave phase speed c_p as $c_p = \omega/k_h$, where ω is the measured angular frequency and k_h is the Pythagorean sum of k and l. We can then calculate the intrinsic frequency, $\hat{\omega}$, given by

$$\hat{\omega} = \omega - k\bar{u} - l\bar{v} \tag{9}$$

where $\bar{u}$ is the background zonal wind and $\bar{v}$ is the background meridional wind. To do this, we use hourly wind values from the radar data linearly interpolated to each image time.

The intrinsic horizontal phase speed, $\hat{c}_p$, can then be computed as $\hat{c}_p = c_p - \bar{u}_h$ where $\bar{u}_h$ is the Pythagorean sum of u and v. Using the medium frequency GW approximation (Fritts & Alexander, 2003), such that the absolute value of vertical wavenumber, m, is given by $|m| = N/|\hat{c}_p|$ where N is the Brunt-Väisälä frequency and $\hat{c}_h$ is the intrinsic horizontal phase speed, this allows us to calculate $\lambda_z = 1/m$.

We can then calculate the intrinsic frequency:

$$\hat{\omega} = N \left| \frac{k_h}{m} \right| \tag{10}$$

and also the intrinsic group speed $\hat{c}_g$:

$$\hat{c}_g = \bar{u} + \frac{\hat{\omega}}{k_h} \tag{11}$$

Once we have performed these calculations we have the following parameters:

- horizontal and vertical wavelengths, λ_h and λ_z, respectively
- observed and intrinsic frequencies, ω and $\hat{\omega}$, respectively
- observed and intrinsic horizontal phase speeds, c_p and $\hat{c}_p$, respectively
- observed and intrinsic group speeds, c_g and $\hat{c}_g$, respectively
- direction
- and finally period T.

4 Results

4.1 Initial Visual Analysis

Figure 4 presents a time series of waves above an S-Transform-derived amplitude threshold over the time period 23:35 to 01:05 on the night of the 26th – 27th of April 2012.

In this figure, to highlight only the strongest wave features results are only shown where the S-Transform output amplitude is above a cutoff value of 200 units, illustrated by a faint semitransparent grey wrapper. This cutoff represents a value close to the 90th percentile of the full measured amplitude distribution including noise-dominated regions. Within this volume, red and blue isosurfaces represent phase fronts of positive and negative perturbations from the background state as the wave moves across the imager's field of view; the outer (semi-transparent) red and blue surfaces enclose values greater than 10 units and the solid inner surfaces values greater than 45 units.

The blue and red isosurfaces can then be interpreted as a visual depiction of the wave's phase fronts as they advance through time. Distinct wavefronts can be seen throughout the chosen period, with the region falling within the amplitude cutoff envelope gradually increasing as the wave covers a larger fraction of the total observed area. We also

see two instances of other waves growing and then dissipating separately to the main wave envelope. We thus conclude that these waves are indeed persistent and large enough to proceed with our investigation.

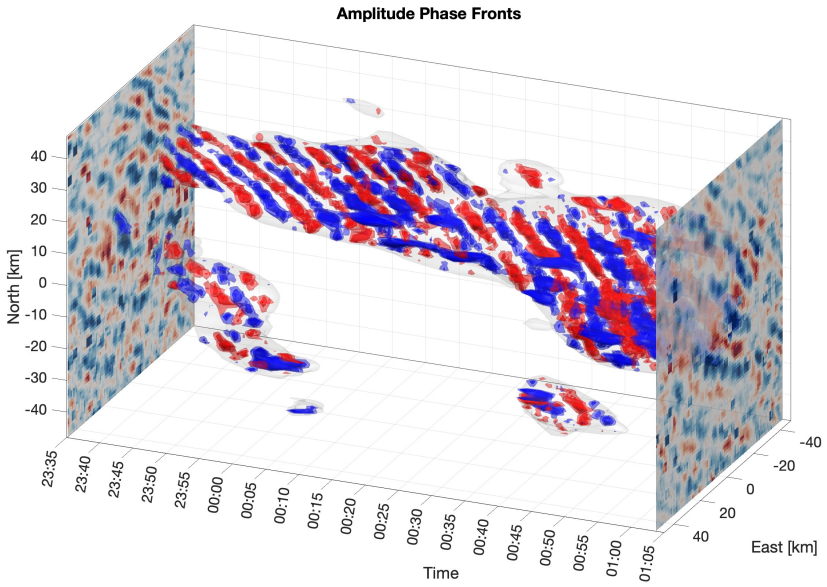

Figure 4. 3D visualisation of wave phase fronts over the time period 23:25 to 01:05 on the night of the 26th – 27th April. Here we have selected waves based on an amplitude threshold. This wave envelope is given in light grey shading around the wave packets. The wave is persistent across the time period and the area of influence increases.

4.2 S-Transform Analysis - Example Results

As described above, from the S-Transform we are able to extract wave amplitude, horizontal wavelengths, frequency and period of each pixel in an image. This allows us to build a picture of the waves and their properties as they vary over time.

Figure 5 presents an example of a single frame from the output of the 3D S-Transform as applied to the airglow imager data over the night of the 26th – 27th April 2012. Figure 5a shows the input data, b the reconstructed wave field based on the output, c the wave amplitude at each point on the image, d the horizontal wavelength calculated as a Pythagorean sum of the wavelengths in the x and y directions, e the direction of propagation and f the period in minutes. It can be seen from this example that the wave seen in the input data and our above time-varying example is clearly detected by the analysis.

In Figure 5a, we can visually identify wave fronts in the image, which are clear to the eye and free from major interference. This means that they are well-placed to be recovered by the S-Transform. A similar picture is seen in Figure 5b, where we reconstruct the detected wave field reconstruction (as described by Hindley et al. (2016)). As this field is visually and quantitatively similar to the input, we can be confident that the wave properties we are calculating using the S-Transform are reliable. In Figure 5c we then show the amplitude calculated for each pixel on the image. We see that the area with more pronounced wave features marked with a black box in Figure 5a – d in the input data exhibits stronger amplitudes than signals in the rest of the figure.

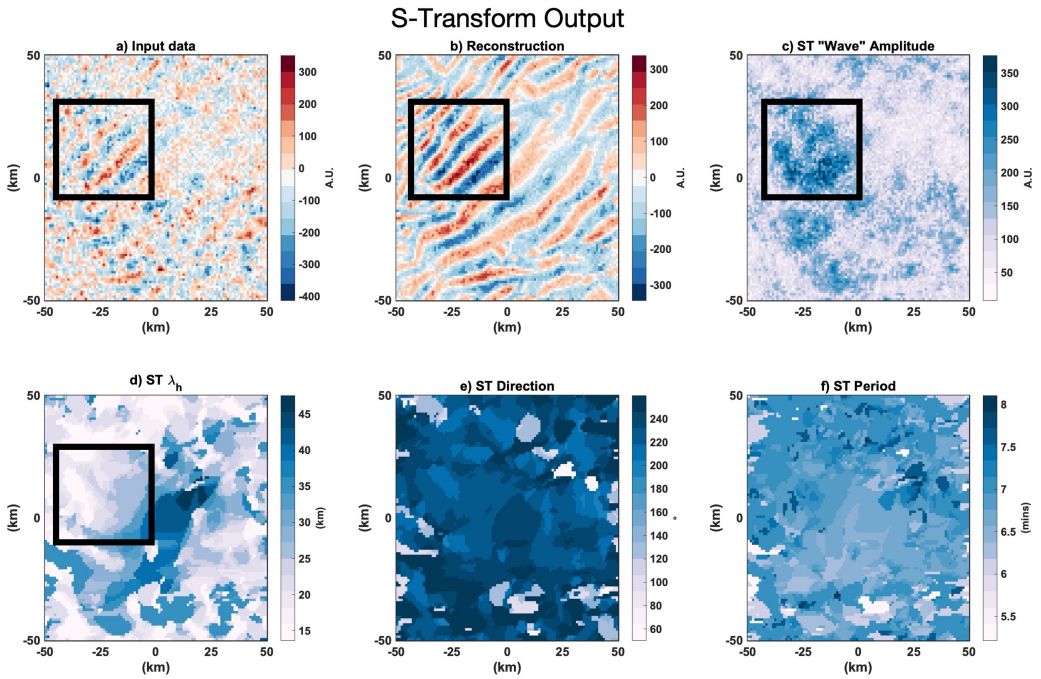

Figure 5. Examples of the S-Transform output. In panel a, the input data following the star and galaxy removal, b presents the reconstruction of the wave field given the wave properties, c shows the amplitude of the wave at each pixel, d presents the horizontal wavelength as a Pythagorean sum of the x and y directions, e direction propagation of the dominant wave at each pixel and f presents the period in minutes.

Further, we show the wavelength in the horizontal direction in Figure 5d. A brief visual check shows that the long wavelengths present in the input data are are picked up by the S-Transform in the reconstruction and in this field. Finally, the periods are shown in Figure 5f ranging from around 5 to 8 minutes. These are fast waves, as the Brunt-Väisälä period at this height is around 5 minutes (Wüst et al., 2017).

4.3 S-Transform Analysis - All-Night Results

We now show integrated results over the entire night. Figure 6 presents histograms of this output, as quantified at the voxel level. Specifically, we have defined this dataset such that each voxel above the 90th percentile threshold used previously for Figure 4 contributes a single count to each histogram. The histograms are defiend across 15 equally-sized bins, with the bin width calculated by computing the range between the maximum and minimum values and dividing this range into 15 equal-width bins. Here we present the horizontal wavelength λ_h in Figure 6a, the vertical wavelength λ_z in b, the angular frequency ω in c, the phase speed c_p in d, the group speed c_g in e, the direction in f, the temporal period T in g, the intrinsic angular frequency $\hat{\omega}$ in h, the intrinsic phase speed $\hat{c_p}$ in i, and the intrinsic group speed $\hat{c_g}$ in j.

The distribution of horizontal wavelengths seen in Figure 6a shows that measured horizontal wavelengths are generally below 30 km. However, there is also a distinct peak at wavelengths ∼35 km. This peak likely arises due to the histograms being computed from voxel-level rather than wave-level data: such a feature is consistent with a promi-

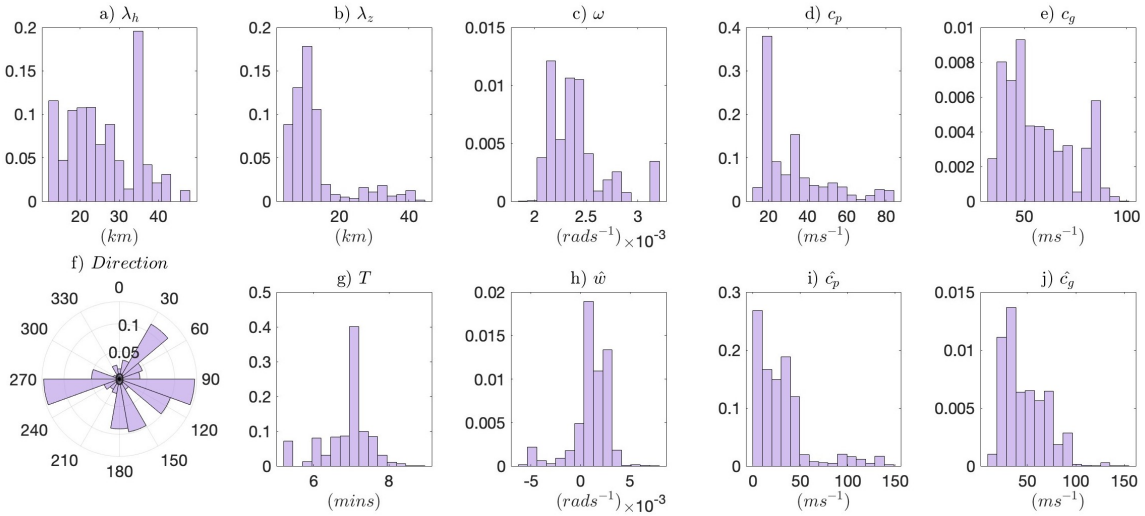

Figure 6. Histograms of the wave properties extracted from the airglow images using the 3D S-Transform for the night of 26th – 27th April 2012. Presented here are the horizontal wavelength λ_h in a), the vertical wavelength λ_z in b), the angular frequency ω in c), the phase speed c_p in d), the group speed c_g in e), the direction in f), the temporal period T in g), the intrinsic angular frequency $\hat{\omega}$ in h), the intrinsic phase speed $\hat{c_p}$ in i), and the intrinsic group speed $\hat{c_g}$ in j).

nent and persistent wave that lasts for multiple frames contibuted a large number of counts in this bin. If we had a method that counted a wave only once as it progressed over the image, we would expect this peak to be less pronounced. However, defining the limits of a wave packet within data of this type is is a non-trivial exercise and developing a method such as this is beyond the scope of this paper.

Vertical wavelengths in Figure 6b shows smaller wavelengths below 20 km are more common than those above 20 km. We can see the peak of this distribution is around 16 km.

The angular frequencies computed for the waves, shown in Figure 6c, suggest a preference for values below 2.5 $rad\ s^{-1}$, but with a noticable secondary peak apparent at values $\sim 3.1\ rad\ s^{-1}$. In Figure 6d the phase speeds show a preference for lower speeds with a peak at 20 ms^{-1} and at 35 ms^{-1}. We can see phase speeds of 15 to 90 ms^{-1}. Larger speeds are, however, less common. The group speed in Figure 6e shows presents two peaks, one at 55 ms^{-1} and one at 90 ms^{-1}. Group speeds between 25 ms^{-1} and 75 ms^{-1} are more common than speeds between 75 ms^{-1} and 100 ms^{-1}, but both are still prominent.

Figure 6f presents the direction of the waves displayed as a bearing (clockwise from north). We can see that some directions are more prominent, i.e. northeast, east-southeast and west-southwest. There are also some waves travelling south.

We present the periods of the waves in Figure 6g where the most common period is at 7 minutes, with periods from 5.5 mins to 8 mins also being present. Above 8 mins, there are limited instances of waves present.

The following parameters are intrinsic wave parameters; that is, they are the wave parameters from the frame of reference of the wind the wave propagates through. In Figure 6h, presenting intrinsic angular frequency, we can see an almost symmetrical distri-

bution surrounding 0 $rad\ s^{-1}$ implying that in the wave frame of reference, waves are travelling both with and against the wind. In Figure 6i, we present the intrinsic phase speed where a preference for lower speeds is evident, specifically below 50 ms^{-1}. Speeds between 100 ms^{-1} and 150 ms^{-1} are observed, but this is a very low occurrence. Finally, intrinsic group speed shows an almost log-normal distribution with speeds between 10 ms^{-1} and 130 ms^{-1} with a peak at around 25 ms^{-1}.

In Figure 6e, we observe group speeds which are large and non-zero. This implies that the waves we see are not only travelling fast but horizontally propagating. This is at odds with common GW parameterisations which consider GWs as being constrained to the vertical column of a single gridbox and which can only propagate vertically within this column (Alexander et al., 2010; Kalisch et al., 2014). These results provide further evidence that this is not the case and that GW parametrisations which do not consider horizontal propagation are unsuitable for capturing these small-scale waves which carry significant quantities of energy and momentum (Geller et al., 2013; Alexander et al., 2010).

5 Discussion

Since in our study we apply a novel method, it is important to assess our results properly in the context of previous work using more conventional approaches. Accordingly, in this section we compare our results quantitatively to previous studies (section 5.1), before discussing the advantages and disadvantages of our approach relative to other available methods (section 5.2).

5.1 Results Comparison to Previous Studies

We have found horizontal wavelengths ranging from around 5 to 45 km, with most voxels being associated with values between 20 – 25 km. This compares favourably with previous studies, which show wavelengths between 20 – 30 km (Kam et al., 2017; Pautet, 2005; Ejiri et al., 2003; Hecht et al., 2001; R. Stockwell et al., 1996), and with peaks at 35 km seen in (Hecht, 2002).

Nielsen et al. (2009) investigated GWs in the hydroxyl airglow layer, using data from when the same imaging system used in our study was deployed instead to the British Antarctic Survey base at Halley, Antarctica (76°S, 27°W). They investigated the seasonal climatology of individual quasi-monochromatic, short-period gravity-wave characteristics at high-southern latitudes. These characteristics were observed over the 2000 and 2001 austral winter seasons. They found horizontal wavelengths from 10 – 70 km, producing a log-normal distribution with a peak at 15 – 20 km. Comparatively, we have observed a range of 10 – 50 km with a high count at 35 km. As we test only a single night of data, this difference may simply be due to the most dominant wave on this specific night having this wavelength. As the S-Transform gives us voxel-level information, not individual wave events, we cannot say how many waves had this wavelength with this information alone.

Similarly, for observed wave periods, we see a range of values from 5 – 9 ms^{-1} with a peak at around 7.5 ms^{-1}. Nielsen et al. (2009) found a range of 5 – 30 ms^{-1} with a log-normal distribution with peak at $\sim$ 7.5 ms^{-1}. This is broadly similar to the peak we have seen, which suggests that this is a common wave period. The wide range of periods seen in their study will come from the two winters of data that have been used. We have used one night to benchmark our method resulting, therefore, in less data and fewer wave events.

The directions observed by Nielsen et al. (2009) showed a clear preference for propagation towards the South Pole, and there is limited evidence of waves propagating North.

Similarly, we have shown that propagation southwards is apparent in our case; however, the directions we observed also peak significantly in the WSW and ESE directions.

Kam et al. (2017) observed a very similar range of observed phase speeds as in our study; however, the periods we observe are faster, with a range from 5 – 9 minutes compared with the range of 5 – 60 minutes in the work of Kam et al. (2017). This also suggests that the results we have uncovered using the 3DST are plausible.

With observed phase speed, Nielsen et al. (2009) saw a range from 0 to 100 ms^{-1} with a peak at 30 to 40 ms^{-1}. This is an almost Gaussian distribution. We observe a range from 10 to 90 ms^{-1}, very similar to that observed at Halley. We also observed a peak at 20 ms^{-1}. This could be a persistent wave event that was spatially large and therefore could be present over many voxels.

5.2 Methodological Comparisons

The addition of supporting meteor radar data also allows is to convert these parameters from the ground-based to the intrinsic frame.

5.2.1 The 2D Stockwell Transform

Here, we apply the 3D Stockwell Transform to data of this type for the first time. The simpler two-dimensional S-Transform (2DST) has however previously been applied to airglow data. Specifically, R. G. Stockwell and Lowe (2001) applied the 2DST to 16 x 16 pixel airglow images, covering a field of view of 1.5 km at the height of the airglow at 87 km. In addition to accounting for time variation, advances in computing power also allow us to work at a much larger scale, allowing us to apply the technique to a full night of observations totalling 360 frames, each of 101 by 101 pixels and hence covering an area of sky equivalent to 100 by 100 km on the surface.

This combination of features allows us to quantify wave parameters over a much larger field of view than (R. G. Stockwell & Lowe, 2001), and to measure many additional parameters. In particular, the ability to simultaneously obtain both spatial information and the temporal frequency of these waves and how they covary is a key advantage over this older 2D approach.

5.2.2 The Fast Fourier Transform

An alternative approach is to use just a 3D FFT without the additional windowing properties of the ST. This is computationally very significantly cheaper. As an example of this approach, Rourke et al. (2017) investigated short-period GWs and ripples at Davis Station, Antarctica (68 °S, 78 °E) using a scanning radiometer to measure hydroxyl airglow perturbations.

The approach of Rourke et al. (2017) identified the dominant wave feature in each frame using the FFT, with the period of the dominant wave determined from time-variations in the FFTs of the weighted centre of 32 successive images centred on the frame in question. Using a sampling rate of 1 min and a maximum window length of 32, the range of wave periods detectable by this approach was 2 to 16 minutes. They then used lag analysis to determine the wave direction and speed.

Our method provides similar outputs, but whereas their approach gave results at the frame level our 3DST approach allows the measurement of geographically-decomposed parameters at the single-voxel level. This allows for more information to be extracted about the waves, and for multiple waves in the same panel to be measured.

5.2.3 Cospectral Analysis

Another method of extracting wave properties is co-spectral analysis, as applied by e.g. Cao and Liu (2022) to airglow images observed at Andes Lidar Observatory (30.3 °S, 70.7 °W) in northern Chile.

In this study, images were unwrapped to a flat field to account for the van Rhijn effect. They removed the galaxy using the Principal Component Analysis (PCA) method from Z. Li et al. (2014), then used three consecutive images to create two time-differenced images. Horizontal wave properties such as wavelength, observed phase speed, direction and relative emission perturbation amplitude were then derived from the co-spectra of the two images, supported as in our study by background winds from a SKiYMET meteor radar system based at the Andes Lidar Observatory to convert between the intrinsic and ground-based frames. Once this step was performed, any wavelengths below 10 km and any periods below the buoyancy frequency were removed.

This method, similar to our 3DST, allowed both observed and intrinsic parameters can be established along with relative emission amplitudes of consecutive images. However, the method also results in some lost information due to taking the direct differences between each frame. Furthermore, it also assumes that the phase difference from voxel to voxel in time is accurate; therefore, any noise present (very likely in real observations) will impact significantly and directly upon the quality of the final results.

5.2.4 The M-Transform

The final method we discuss is the M-Transform. This was formulated by Matsuda et al. (2014) as a 3D method to extract wave properties, similar in underlying conception to the S-Transform.

As with the S-Transform, the M-Transform requires a time series of airglow images with fixed and consistent pixel time spacing. For this method, once again, the airglow images must be preprocessed to remove stars, the galaxy, and any lens effects, and must also be projected onto geographic coordinates. Once this has been done, the M-transform transforms the Power Spectral Density (PSD) in the wavenumber domain (k, l, ω), where k and l are the wavenumbers in the zonal and meridional direction, respectively and ω is the frequency in the phase velocity domain (v_x, v_y, ω) via the following equations:

$$v_x = \frac{\omega k}{k^2 + l^2} \tag{12}$$

$$v_y = \frac{\omega l}{k^2 + l^2} \tag{13}$$

Where v_x and v_y are the orthogonal projections of the phase velocity onto zonal and meridional axes, respectively. This allows for the calculation of phase speed and azimuth as:

$$(v_x, v_y) = c(sin\phi, cos\phi) \tag{14}$$

Where c is the phase speed, and ϕ is the azimuth. Finally, the phase velocity is integrated to give a 2D phase velocity spectrum.

The M-transform shares many benefits with the S-Transform method we present in this study. For instance, it is highly automated and does not require interaction with the user, it is 3D, and it provides many wave properties directly. However, the M-transform is statistical, and there is no information provided from the analysis about specific locations and times within the dataset used - all properties are measured at the bulk level for the whole dataset. The ability of the S-Transform approach to resolve the same properties at the voxel level is thus a significant advantage.

6 Conclusions

In this study, we have presented a new application of a 3D spectral analysis technique, the 3D S-Transform, to airglow imager data from the Antarctic Peninsula at the British Antarctic Survey Base at Rothera (68°S, 68°W).

The method is automated and can identify wave properties for each pixel; we can, therefore, use it to investigate the spatial extent of the wave, as in Figure 4.

We have found that:

1. The 3D S-Transform method works well with processed airglow imager data and measures wave parameters consistent with the airglow literature
2. The majority of waves seen in the airglow in this case study are small, fast GWs with short periods.
3. We see a distribution of horizontal wavelengths between 10 to 50 km with a sharp peak at 35 km, possibly due to methodological reasons
4. Vertical wavelengths peak at values below 20 km, peaking at around 15 km but with the largest peak at around 40 km.
5. Phase speeds are generally low, and group speeds are high and non-zero This suggests that the waves observed are travelling horizontally and also fast, further suggesting that GW parametrisations which do not account for horizontal movement are inadequate
6. Finally, we can give accurate locations of where the waves in the airglow are present due to the 3D S-Transform investigating waves on the pixel rather than wave event level.

Future studies could advantageously use the S-Transform in tandem with an automated image processing technique to improve the process thus allowing the identification of airglow images that are of sufficient clarity for use in the investigation of GWs. Used together, these processes would allow airglow images to be processed and analysed in one programme with little input from the user, allowing for a fully automated process. This would result in GW parameters and their locations on each frame. More work on the spatial extent of the wave could then be performed and investigated.

Data Availability

The meteor radar data used in this study are archived as part of from Mitchell, N. (2019): University of Bath: Rothera Skiymet Meteor Radar data (2005 – present). Centre for Environmental Data Analysis, 2022. `https://catalogue.ceda.ac.uk/uuid/aa44e02718fd4ba49cefe36d884c6e5`

Acknowledgments
SMD is supported by a NERC GW4+ Doctoral Training Partnership studentship from the Natural Environment Research Council (NERC, grant number NE/L002434/1). TMG, CJW and NJM are supported by NERC (NE/R001391/1 and NE/R001235/1) and CJW by a Royal Society University Research Fellowship (URF\R\221023)

CRediT authorship contribution statement

Conceptualisation: CJW and NJM; Data curation: SMD, NPH, TM-G, P-DP and MJT; Formal analysis: SMD and NPH; Investigation: SMD and NPH; Methodology: SMD, NPH, CJW and NJM; Project administration: CJW; Resources: CJW, NJM and TM-G; Software: SMD and NPH; Supervision: CJW, NJM and TM-G; Validation: NPH, CJW, NJM and TM-G; Visualization: SMD and CJW; Writing – original draft: SMD; Writing - review and editing: SMD, NPH, CJW and TM-G.

References

Alexander, M. J., Geller, M., McLandress, C., Polavarapu, S., Preusse, P., Sassi, F., ... Watanabe, S. (2010, July). Recent developments in gravity-wave effects in climate models and the global distribution of gravity-wave momentum flux from observations and models. *Quarterly Journal of the Royal Meteorological Society*, *136*(650), 1103–1124. Retrieved from https://doi.org/10.1002/qj.637 doi: 10.1002/qj.637

Alexander, M. J., & Teitelbaum, H. (2007, November). Observation and analysis of a large amplitude mountain wave event over the antarctic peninsula. *Journal of Geophysical Research*, *112*(D21). Retrieved from https://doi.org/10.1029/2006jd008368 doi: 10.1029/2006jd008368

Baker, D. J., & Stair, A. T. (1988, April). Rocket measurements of the altitude distributions of the hydroxyl airglow. *Physica Scripta*, *37*(4), 611–622. Retrieved from https://doi.org/10.1088/0031-8949/37/4/021 doi: 10.1088/0031-8949/37/4/021

Baumgaertner, A. J. G., & McDonald, A. J. (2007, March). A gravity wave climatology for antarctica compiled from challenging minisatellite payload/global positioning system (CHAMP/GPS) radio occultations. *Journal of Geophysical Research*, *112*(D5). Retrieved from https://doi.org/10.1029/2006jd007504 doi: 10.1029/2006jd007504

Becker, E. (2012, October). Dynamical control of the middle atmosphere. *Space Science Reviews*, *168*(1-4), 283–314. Retrieved from https://doi.org/10.1007/s11214-011-9841-5 doi: 10.1007/s11214-011-9841-5

Beldon, C., Muller, H., & Mitchell, N. (2006, March). The 8-hour tide in the mesosphere and lower thermosphere over the UK, 1988–2004. *Journal of Atmospheric and Solar-Terrestrial Physics*, *68*(6), 655–668. Retrieved from https://doi.org/10.1016/j.jastp.2005.10.004 doi: 10.1016/j.jastp.2005.10.004

Cao, B., & Liu, A. Z. (2016, January). Intermittency of gravity wave momentum flux in the mesopause region observed with an all-sky airglow imager. *Journal of Geophysical Research: Atmospheres*, *121*(2), 650–663. Retrieved from https://doi.org/10.1002/2015jd023802 doi: 10.1002/2015jd023802

Cao, B., & Liu, A. Z. (2022, June). Statistical characteristics of high-frequency gravity waves observed by an airglow imager at andes lidar observatory. *Earth and Space Science*, *9*(6). Retrieved from https://doi.org/10.1029/2022ea002256 doi: 10.1029/2022ea002256

Davis, R. N., Du, J., Smith, A. K., Ward, W. E., & Mitchell, N. J. (2013, September). The diurnal and semidiurnal tides over ascension island (° s, 14° w) and their interaction with the stratospheric quasi-biennial oscillation: studies with meteor radar, eCMAM and WACCM. *Atmospheric Chemistry and Physics*, *13*(18), 9543–9564. Retrieved from https://doi.org/10.5194/acp-13-9543-2013 doi: 10.5194/acp-13-9543-2013

Dempsey, S. M., Hindley, N. P., Moffat-Griffin, T., Wright, C. J., Smith, A. K., Du, J., & Mitchell, N. J. (2021, January). Winds and tides of the antarctic mesosphere and lower thermosphere: One year of meteor-radar observations over rothera (68°s, 68°w) and comparisons with WACCM and eCMAM. *Journal of Atmospheric and Solar-Terrestrial Physics*, *212*, 105510. Retrieved from https://doi.org/10.1016/j.jastp.2020.105510 doi: 10.1016/j.jastp.2020.105510

Ejiri, M. K., Shiokawa, K., Ogawa, T., Igarashi, K., Nakamura, T., & Tsuda, T. (2003, November). Statistical study of short-period gravity waves in OH and OI nightglow images at two separated sites. *Journal of Geophysical Research: Atmospheres*, *108*(D21). Retrieved from https://doi.org/10.1029/2002jd002795 doi: 10.1029/2002jd002795

Fritts, D. C., & Alexander, M. J. (2003, March). Gravity wave dynamics and ef-

fects in the middle atmosphere. *Reviews of Geophysics*, *41*(1). Retrieved from https://doi.org/10.1029/2001rg000106 doi: 10.1029/2001rg000106

Fritts, D. C., Vadas, S. L., Wan, K., & Werne, J. A. (2006, February). Mean and variable forcing of the middle atmosphere by gravity waves. *Journal of Atmospheric and Solar-Terrestrial Physics*, *68*(3-5), 247–265. Retrieved from https://doi.org/10.1016/j.jastp.2005.04.010 doi: 10.1016/j.jastp.2005.04.010

Ganaie, B. A., Ramkumar, T., Bhat, A. H., & Malik, M. A. (2022, July). Imager observation of concentric mesospheric gravity waves over srinagar, jammu and kashmir, india. *Advances in Space Research*, *70*(2), 427–439. Retrieved from https://doi.org/10.1016/j.asr.2022.04.035 doi: 10.1016/j.asr.2022.04.035

Gardner, C. S., & Taylor, M. J. (1998). Observational limits for lidar, radar, and airglow imager measurements of gravity wave parameters. *Journal of Geophysical Research: Atmospheres*, *103*(D6), 6427-6437. Retrieved from https://agupubs.onlinelibrary.wiley.com/doi/abs/10.1029/97JD03378 doi: https://doi.org/10.1029/97JD03378

Geller, M. A., Alexander, M. J., Love, P. T., Bacmeister, J., Ern, M., Hertzog, A., ... Zhou, T. (2013, August). A comparison between gravity wave momentum fluxes in observations and climate models. *Journal of Climate*, *26*(17), 6383–6405. Retrieved from https://doi.org/10.1175/jcli-d-12-00545.1 doi: 10.1175/jcli-d-12-00545.1

Goldberg, R. A. (2004). The MaCWAVE/MIDAS rocket and ground-based measurements of polar summer dynamics: Overview and mean state structure. *Geophysical Research Letters*, *31*(24). Retrieved from https://doi.org/10.1029/2004gl019411 doi: 10.1029/2004gl019411

Hecht, J. H. (2002). An observation of a fast external atmospheric acoustic-gravity wave. *Journal of Geophysical Research*, *107*(D20). Retrieved from https://doi.org/10.1029/2001jd001438 doi: 10.1029/2001jd001438

Hecht, J. H., Walterscheid, R. L., Hickey, M. P., & Franke, S. J. (2001, March). Climatology and modeling of quasi-monochromatic atmospheric gravity waves observed over urbana illinois. *Journal of Geophysical Research: Atmospheres*, *106*(D6), 5181–5195. Retrieved from https://doi.org/10.1029/2000jd900722 doi: 10.1029/2000jd900722

Hindley, N. P., Cobbett, N., Fritts, D. C., Janchez, D., Mitchell, N. J., Moffat-Griffin, T., ... Wright, C. J. (2022, December). Radar observations of winds, waves and tides in the mesosphere and lower thermosphere over south georgia island (54°s, 36°w) and comparison to WACCM simulations. *ACP*. Retrieved from https://doi.org/10.5194/acp-2021-981 doi: 10.5194/acp-2021-981

Hindley, N. P., Smith, N. D., Wright, C. J., Rees, D. A. S., & Mitchell, N. J. (2016, June). A two-dimensional stockwell transform for gravity wave analysis of AIRS measurements. *Atmospheric Measurement Techniques*, *9*(6), 2545–2565. Retrieved from https://doi.org/10.5194/amt-9-2545-2016 doi: 10.5194/amt-9-2545-2016

Hindley, N. P., Wright, C. J., Smith, N. D., Hoffmann, L., Holt, L. A., Alexander, M. J., ... Mitchell, N. J. (2019, December). Gravity waves in the winter stratosphere over the southern ocean: high-resolution satellite observations and 3-d spectral analysis. *Atmospheric Chemistry and Physics*, *19*(24), 15377–15414. Retrieved from https://doi.org/10.5194/acp-19-15377-2019 doi: 10.5194/acp-19-15377-2019

Hindley, N. P., Wright, C. J., Smith, N. D., & Mitchell, N. J. (2015, July). The southern stratospheric gravity wave hot spot: individual waves and their momentum fluxes measured by COSMIC GPS-RO. *Atmospheric Chemistry and Physics*, *15*(14), 7797–7818. Retrieved from https://doi.org/10.5194/acp-15-7797-2015 doi: 10.5194/acp-15-7797-2015

Hocking, W., Fuller, B., & Vandepeer, B. (2001, January). Real-time determination of meteor-related parameters utilizing modern digital technology. *Journal of Atmospheric and Solar-Terrestrial Physics*, *63*(2-3), 155–169. Retrieved from https://doi.org/10.1016/s1364-6826(00)00138-3 doi: 10.1016/s1364-6826(00)00138-3

Hu, S., Ma, S., Yan, W., Hindley, N. P., Xu, K., & Jiang, J. (2019a, January). Measuring gravity wave parameters from a nighttime satellite low-light image based on two-dimensional stockwell transform. *Journal of Atmospheric and Oceanic Technology*, *36*(1), 41–51. Retrieved from https://doi.org/10.1175/jtech-d-18-0092.1 doi: 10.1175/jtech-d-18-0092.1

Hu, S., Ma, S., Yan, W., Hindley, N. P., Xu, K., & Jiang, J. (2019b, January). Measuring gravity wave parameters from a nighttime satellite low-light image based on two-dimensional stockwell transform. *Journal of Atmospheric and Oceanic Technology*, *36*(1), 41–51. Retrieved from https://doi.org/10.1175/jtech-d-18-0092.1 doi: 10.1175/jtech-d-18-0092.1

Hu, S., Ma, S., Yan, W., Hindley, N. P., & Zhao, X. (2019, April). Measuring internal solitary wave parameters based on VIIRS/DNB data. *International Journal of Remote Sensing*, *40*(20), 7805–7816. Retrieved from https://doi.org/10.1080/01431161.2019.1608389 doi: 10.1080/01431161.2019.1608389

Kalisch, S., Preusse, P., Ern, M., Eckermann, S. D., & Riese, M. (2014). Differences in gravity wave drag between realistic oblique and assumed vertical propagation. *Journal of Geophysical Research: Atmospheres*, *119*(17), 10,081-10,099. Retrieved from https://agupubs.onlinelibrary.wiley.com/doi/abs/10.1002/2014JD021779 doi: https://doi.org/10.1002/2014JD021779

Kam, H., Jee, G., Kim, Y., bae Ham, Y., & Song, I.-S. (2017, March). Statistical analysis of mesospheric gravity waves over king sejong station, antarctica (62.2°s, 58.8°w). *Journal of Atmospheric and Solar-Terrestrial Physics*, *155*, 86–94. Retrieved from https://doi.org/10.1016/j.jastp.2017.02.006 doi: 10.1016/j.jastp.2017.02.006

Khomich, V. Y., Semenov, A. I., & Shefov, N. N. (2008). *Airglow as an indicator of upper atmospheric structure and dynamics*. Springer Science & Business Media.

Kogure, M., Yue, J., & Liu, H. (2021, April). Gravity wave weakening during the 2019 antarctic stratospheric sudden warming. *Geophysical Research Letters*, *48*(8). Retrieved from https://doi.org/10.1029/2021gl092537 doi: 10.1029/2021gl092537

Kogure, M., Yue, J., Nakamura, T., Hoffmann, L., Vadas, S. L., Tomikawa, Y., ... Janches, D. (2020, September). First direct observational evidence for secondary gravity waves generated by mountain waves over the andes. *Geophysical Research Letters*, *47*(17). Retrieved from https://doi.org/10.1029/2020gl088845 doi: 10.1029/2020gl088845

Li, J., Li, T., Dou, X., Fang, X., Cao, B., She, C.-Y., ... Thorsen, D. (2017, March). Characteristics of ripple structures revealed in OH airglow images. *Journal of Geophysical Research: Space Physics*, *122*(3), 3748–3759. Retrieved from https://doi.org/10.1002/2016ja023538 doi: 10.1002/2016ja023538

Li, Z., Liu, A., & Sivjee, G. G. (2014, April). Removing milky way from airglow images using principal component analysis. *Journal of Atmospheric and Solar-Terrestrial Physics*, *110-111*, 50–57. Retrieved from https://doi.org/10.1016/j.jastp.2014.01.016 doi: 10.1016/j.jastp.2014.01.016

Li, Z., Liu, A. Z., Lu, X., Swenson, G. R., & Franke, S. J. (2011, November). Gravity wave characteristics from OH airglow imager over maui. *Journal of Geophysical Research: Atmospheres*, *116*(D22), n/a–n/a. Retrieved from https://doi.org/10.1029/2011jd015870 doi: 10.1029/2011jd015870

Lindzen, R. S. (1981). Turbulence and stress owing to gravity wave and tidal breakdown. *Journal of Geophysical Research*, *86*(C10), 9707. Retrieved from

https://doi.org/10.1029/jc086ic10p09707 doi: 10.1029/jc086ic10p09707

Matsuda, T. S., Nakamura, T., Ejiri, M. K., Tsutsumi, M., & Shiokawa, K. (2014, August). New statistical analysis of the horizontal phase velocity distribution of gravity waves observed by airglow imaging. *Journal of Geophysical Research: Atmospheres*, *119*(16), 9707–9718. Retrieved from https://doi.org/10.1002/2014jd021543 doi: 10.1002/2014jd021543

McDonald, A. J. (2012, August). Gravity wave occurrence statistics derived from paired COSMIC/FORMOSAT3 observations. *Journal of Geophysical Research: Atmospheres*, *117*(D15), n/a–n/a. Retrieved from https://doi.org/10.1029/2011jd016715 doi: 10.1029/2011jd016715

Meinel, I. A. B. (1950, May). OH emission bands in the spectrum of the night sky. *The Astrophysical Journal*, *111*, 555. Retrieved from https://doi.org/10.1086/145296 doi: 10.1086/145296

Miller, S. D., Straka, W. C., Yue, J., Smith, S. M., Alexander, M. J., Hoffmann, L., ... Partain, P. T. (2015, November). Upper atmospheric gravity wave details revealed in nightglow satellite imagery. *Proceedings of the National Academy of Sciences*, *112*(49). Retrieved from https://doi.org/10.1073/pnas.1508084112 doi: 10.1073/pnas.1508084112

Mitchell, N. J. (2002). Mean winds and tides in the arctic mesosphere and lower thermosphere. *Journal of Geophysical Research*, *107*(A1). Retrieved from https://doi.org/10.1029/2001ja900127 doi: 10.1029/2001ja900127

Moffat-Griffin, T., & Colwell, S. R. (2017, September). The characteristics of the lower stratospheric gravity wavefield above halley (75°s, 26°w), antarctica, from radiosonde observations. *Journal of Geophysical Research: Atmospheres*, *122*(17), 8998–9010. Retrieved from https://doi.org/10.1002/2017jd027079 doi: 10.1002/2017jd027079

Nielsen, K. (2007). *Climatology and case studies of mesospheric gravity waves observed at polar latitudes*. Utah State University.

Nielsen, K., Taylor, M., Hibbins, R., & Jarvis, M. (2009, June). Climatology of short-period mesospheric gravity waves over halley, antarctica (76°s, 27°w). *Journal of Atmospheric and Solar-Terrestrial Physics*, *71*(8-9), 991–1000. Retrieved from https://doi.org/10.1016/j.jastp.2009.04.005 doi: 10.1016/j.jastp.2009.04.005

Nielsen, K., Taylor, M. J., Pautet, P.-D., Fritts, D. C., Mitchell, N., Beldon, C., ... Goldberg, R. A. (2006, July). Propagation of short-period gravity waves at high-latitudes during the MaCWAVE winter campaign. *Annales Geophysicae*, *24*(4), 1227–1243. Retrieved from https://doi.org/10.5194/angeo-24-1227-2006 doi: 10.5194/angeo-24-1227-2006

Pautet, P.-D. (2005). Climatology of short-period gravity waves observed over northern australia during the darwin area wave experiment (DAWEX) and their dominant source regions. *Journal of Geophysical Research*, *110*(D3). Retrieved from https://doi.org/10.1029/2004jd004954 doi: 10.1029/2004jd004954

Perrett, J. A., Wright, C. J., Hindley, N. P., Hoffmann, L., Mitchell, N. J., Preusse, P., ... Eckermann, S. D. (2021, January). Determining gravity wave sources and propagation in the southern hemisphere by ray-tracing AIRS measurements. *Geophysical Research Letters*, *48*(2). Retrieved from https://doi.org/10.1029/2020gl088621 doi: 10.1029/2020gl088621

Peterson, A. W. (1979, Oct). Airglow events visible to the naked eye. *Appl. Opt.*, *18*(20), 3390–3393. Retrieved from http://opg.optica.org/ao/abstract.cfm?URI=ao-18-20-3390 doi: 10.1364/AO.18.003390

Rourke, S., Mulligan, F. J., French, W. J. R., & Murphy, D. J. (2017). A climatological study of short-period gravity waves and ripples at davis station, antarctica (68°s, 78°e), during the (austral winter february–october) period 1999–2013. *Journal of Geophysical Research: Atmospheres*, *122*(21), 11,388-

11,404. Retrieved from https://agupubs.onlinelibrary.wiley.com/doi/abs/10.1002/2017JD026998 doi: https://doi.org/10.1002/2017JD026998

Sedlak, R., Zuhr, A., Schmidt, C., Wüst, S., Bittner, M., Didebulidze, G. G., & Price, C. (2020, September). Intra-annual variations of spectrally resolved gravity wave activity in the upper mesosphere/lower thermosphere (UMLT) region. *Atmospheric Measurement Techniques*, *13*(9), 5117–5128. Retrieved from https://doi.org/10.5194/amt-13-5117-2020 doi: 10.5194/amt-13-5117-2020

Stober, G., Kuchar, A., Pokhotelov, D., Liu, H., Liu, H.-L., Schmidt, H., ... Mitchell, N. (2021, September). Interhemispheric differences of mesosphere–lower thermosphere winds and tides investigated from three whole-atmosphere models and meteor radar observations. *Atmospheric Chemistry and Physics*, *21*(18), 13855–13902. Retrieved from https://doi.org/10.5194/acp-21-13855-2021 doi: 10.5194/acp-21-13855-2021

Stockwell, R., Mansinha, L., & Lowe, R. (1996). Localization of the complex spectrum: the s transform. *IEEE Transactions on Signal Processing*, *44*(4), 998-1001. doi: 10.1109/78.492555

Stockwell, R. G., & Lowe, R. P. (2001, August). Airglow imaging of gravity waves: 1. results from a small network of OH nightglow scanning imagers. *Journal of Geophysical Research: Atmospheres*, *106*(D15), 17185–17203. Retrieved from https://doi.org/10.1029/2001jd900035 doi: 10.1029/2001jd900035

Takahashi, H., Melo, S. M. L., Clemesha, B. R., Simonich, D. M., Stegman, J., & Witt, G. (1996, February). Atomic hydrogen and ozone concentrations derived from simultaneous lidar and rocket airglow measurements in the equatorial region. *Journal of Geophysical Research: Atmospheres*, *101*(D2), 4033–4040. Retrieved from https://doi.org/10.1029/95jd03035 doi: 10.1029/95jd03035

Taylor, M. J., Pendleton, W. R., Clark, S., Takahashi, H., Gobbi, D., & Goldberg, R. A. (1997, November). Image measurements of short-period gravity waves at equatorial latitudes. *Journal of Geophysical Research: Atmospheres*, *102*(D22), 26283–26299. Retrieved from https://doi.org/10.1029/96jd03515 doi: 10.1029/96jd03515

Taylor, M. J., Ryan, E. H., Tuan, T. F., & Edwards, R. (1993, April). Evidence of preferential directions for gravity wave propagation due to wind filtering in the middle atmosphere. *Journal of Geophysical Research: Space Physics*, *98*(A4), 6047–6057. Retrieved from https://doi.org/10.1029/92ja02604 doi: 10.1029/92ja02604

von Savigny, C. (2015, May). Variability of OH(3–1) emission altitude from 2003 to 2011: Long-term stability and universality of the emission rate–altitude relationship. *Journal of Atmospheric and Solar-Terrestrial Physics*, *127*, 120–128. Retrieved from https://doi.org/10.1016/j.jastp.2015.02.001 doi: 10.1016/j.jastp.2015.02.001

Wright, C. J., & Gille, J. C. (2013, May). Detecting overlapping gravity waves using the s-transform. *Geophysical Research Letters*, *40*(9), 1850–1855. Retrieved from https://doi.org/10.1002/grl.50378 doi: 10.1002/grl.50378

Wright, C. J., Hindley, N. P., Hoffmann, L., Alexander, M. J., & Mitchell, N. J. (2017, July). Exploring gravity wave characteristics in 3-d using a novel s-transform technique: AIRS/aqua measurements over the southern andes and drake passage. *Atmospheric Chemistry and Physics*, *17*(13), 8553–8575. Retrieved from https://doi.org/10.5194/acp-17-8553-2017 doi: 10.5194/acp-17-8553-2017

Wüst, S., & Bittner, M. (2008, March). Gravity wave reflection: Case study based on rocket data. *Journal of Atmospheric and Solar-Terrestrial Physics*, *70*(5), 742–755. Retrieved from https://doi.org/10.1016/j.jastp.2007.10.010 doi: 10.1016/j.jastp.2007.10.010

Wüst, S., Bittner, M., Espy, P. J., French, W. J. R., & Mulligan, F. J. (2022, Au-

gust). Hydroxyl airglow observations for investigating atmospheric dynamics: results and challenges. *Atmospheric Chemistry and Physics*. Retrieved from https://doi.org/10.5194/acp-2022-528 doi: 10.5194/acp-2022-528

Wüst, S., Bittner, M., Yee, J.-H., Mlynczak, M. G., & III, J. M. R. (2017, December). Variability of the brunt-väisälä frequency at the OH* layer height. *Atmospheric Measurement Techniques*, *10*(12), 4895–4903. Retrieved from https://doi.org/10.5194/amt-10-4895-2017 doi: 10.5194/amt-10-4895-2017

Wüst, S., Wendt, V., Schmidt, C., Lichtenstern, S., Bittner, M., Yee, J.-H., ... III, J. M. R. (2016, February). Derivation of gravity wave potential energy density from NDMC measurements. *Journal of Atmospheric and Solar-Terrestrial Physics*, *138-139*, 32–46. Retrieved from https://doi.org/10.1016/j.jastp.2015.12.003 doi: 10.1016/j.jastp.2015.12.003

Yoshimura, R., Iwagami, N., & Oyama, K.-I. (2003, September). Rocket measurement of electron density and atomic oxygen density modulated by atmospheric gravity waves. *Advances in Space Research*, *32*(5), 837–842. Retrieved from https://doi.org/10.1016/s0273-1177(03)00422-8 doi: 10.1016/s0273-1177(03)00422-8